METRICA
METRology Institutional CAtalog

ISTITUTO NAZIONALE DI RICERCA METROLOGICA
Repository Istituzionale

A Full Physical Strategy for Electrical Contacts on Laser-Induced Graphene (LIG) Electrodes

Original
A Full Physical Strategy for Electrical Contacts on
Laser-Induced Graphene (LIG) Electrodes / Arcoraci, D., Martellone, S., Miceli, M., Molino, D., Ribotta, L., Mossotti, G., Testa, A., Bertana, V., Scaltrito, L., Lamberti, A.. - In: ADVANCED ELECTRONIC MATERIALS. - ISSN 2199-160X. - (2026). [10.1002/aelm.70576]

Availability:
This version is available at: 11696/90559 since: 2026-10-27T05:13:36Z

Publisher:
Wiley

Published
DOI:10.1002/aelm.70576

Terms of use:

This article is made available under terms and conditions as specified in the corresponding bibliographic description in the repository

Publisher copyright

(Article begins on next page)

24 November 2026

Check for updates

Advanced Electronic Materials

ADVANCED ELECTRONIC MATERIALS Open Access

www.advelectronicmat.de

RESEARCH ARTICLE OPEN ACCESS

A Full Physical Strategy for Electrical Contacts on Laser-Induced Graphene (LIG) Electrodes

Davide Arcoraci[1] | Simone Martellone[2] | Michele Miceli[1] | Davide Molino[2] | Luigi Ribotta[3] | Giulia Mossotti[1] | Alessio Testa[4] | Valentina Bertana[1,5] | Luciano Scaltrito[1] | Andrea Lamberti[1,2]

[1]Department of Applied Science and Technology, DISAT, Politecnico di Torino, Torino, Italia | [2]Istituto Italiano di Tecnologia, Centre for Sustainable Future Technology, Torino, Italia | [3]Applied Metrology and Engineering Division, Istituto Nazionale di Ricerca Metrologica (INRiM), Torino, Italia | [4]Microla Optoelectronics S.r.l., Torino, Italia | [5]Chilab-ITEM, DISAT, Politecnico di Torino, Torino, Italia

Correspondence: Davide Arcoraci (davide_arcoraci@polito.it) | Andrea Lamberti (andrea.lamberti@iit.it)

Received: 28 April 2026 | **Revised:** 24 July 2026 | **Accepted:** 1 September 2026

Keywords: laser induced graphene | LIG | metal micro-patterning contacts | micro-supercapacitors | sheet resistance

ABSTRACT

Laser-induced graphene (LIG) has emerged as a highly promising material for energy storage devices due to its excellent electrical conductivity, high specific surface area, and compatibility with flexible substrates. Despite these advantages, one of the main challenges in implementing LIG-based electrodes is achieving a stable and efficient electrical connection with metallic current collectors without compromising the intrinsic properties of the material. In this study, we investigate a combination of physical approaches to establish a reliable and robust electrical bond between LIG and metal current collectors while avoiding chemical treatments, conductive adhesives, or binders. Electrode fabrication is performed using physical vapor deposition (PVD) and laser processing techniques, which provide precise control over both metallic layer deposition and LIG formation. These methods enable straightforward customization of electrode architectures for applications, including symmetric and hybrid energy storage devices. Furthermore, fast and selective laser treatments are adopted to enhance the mechanical integrity and long-term stability of the electrode interfaces. Our results demonstrate a contact resistance as low as 1.3 Ω at the LIG-gold interface without the use of binders or additional conductive agents. The proposed fabrication strategy improves electrical performance while simplifying the overall manufacturing process. By minimizing complex chemical procedures, it enables scalability.

1 | Introduction

In recent years, Laser-Induced Graphene (LIG) has established itself as one of the most versatile materials for the realization of energy storage devices, thanks to the combination of unique properties such as high electrical conductivity, large specific surface area, and compatibility with both flexible and rigid substrates. However, a major limitation of LIG-based devices lies in the formation of reliable electrical contacts. Traditional approaches to electrode integration often result in poor ohmic contact, increased resistance, and reduced device performance. In this paper, we demonstrate how it is possible to improve the chemical compatibility of the mentioned material, reduce contact resistance, and significantly simplify both the design and the production of electrodes for energy storage devices. Moreover, the results presented here are intended to provide a scalable, efficient technological base, compatible with the compatibility requirements of systems integrated on board. At

Abbreviations: CV, Cyclic Voltammetry; EDLC, Electrochemical Double Layer Capacitance; EDX, X-Rays Electron Diffraction; EIS, Electrochemical Impedance Spectroscopy; GCPL, Galvanostatic Charge Potential Limitation; GLM, Graphene Like Material; LIG, Laser Induced Graphene; PCB, Printed Circuit Board; PI, Polyimmide; PVD, Physical Vapor Deposition; SC, Super Capacitor; SEM, Scansion Electron Microscopy.

This is an open access article under the terms of the Creative Commons Attribution License, which permits use, distribution and reproduction in any medium, provided the original work is properly cited.

© 2026 The Author(s). *Advanced Electronic Materials* published by Wiley-VCH GmbH

this point, the question remains: why do we need to implant and contact, on an electronic PCB board, an object with high surface area? Implanting high-capacitance-density points on an electronic board can entail several advantages. Such as storing charge/energy for time intervals with a range from tens of seconds to a minute, therefore acting as short-term storage or as a buffer, and also let to install sensitive materials to detect physical changes [1]. The miniaturization of supercapacitors and the use of micro-supercapacitors [2] are crucial in fields such as sensor technology [3, 4], wearable electronics [5–7], power electronics, and more generally in self-powered devices that coexist with harvesting modules and low-power storage [8, 9].

In general, LIG elements are obtained by converting a polymeric substrate into graphene-like material [10]. In particular, pulsed laser writing enables the local conversion of substrates like polyimide (PI) into a porous graphene-like carbon structure, producing conductive patterns with high surface area and mechanical flexibility. A first proposal of conversion from commercial materials was given by [10], subsequently by [11, 12]. Although nowadays the conversion of polymeric materials into graphene-based materials is well understood, most research has focused on surface functionalization in order to enhance the LIG electrochemical performance. Currently, the integration of this material is still challenging [13–16], and no relevant works are present in the literature.

Despite its potential, contacting LIG in practical devices represents a critical point. Traditional methods based on adhesives or chemical treatments [17] can compromise the intrinsic properties of the material, introduce parasitic resistances or elements of contamination for electrochemistry, or limit the scalability of the production process. In fact, in the literature, it is possible to find different methods to obtain electrical contacts on LIG electrodes, and these can be grouped into three categories, each of which has specific limitations. One approach is the deposition of metal, typically by sputtering gold or other conductive metals directly onto the surface of the LIG. This method presents significant challenges due to the intrinsic porous morphology of LIG. Indeed, LIG is highly porous with considerable surface roughness, and metal deposition via sputtering or evaporation may coat mostly the outermost features of the porous network, limiting penetration into the bulk porous structure and reducing the effective contact area [18]. Furthermore, this method requires the use of a physical mask or lithographic patterning, increasing the complexity and the cost of this approach. The second category relies on the use of conductive pastes, with multiple step preparation, such as silver epoxy or carbon paste. These are simple to apply but have significant drawbacks in electronic and electrochemical systems. For example, mounting SMDs components on LIG stripes is still an open issue. Lead soldering is impractical, the conductive epoxy adhesive does not provide robust adhesion, risk for cracks [19], and suffer of non-negligible contact resistance [20]. Moreover, acidic environments pose a serious problem for silver paste, leading to the dissolution of the contact, while carbon pastes suffer of unstable contact resistance and low conductivity [21]. The third approach, namely mechanical clamping, is mostly used in laboratory scale, but it is incompatible with device miniaturization or scalable manufacturing and produces contact resistances that are sensitive to applied pressure and therefore poorly reproducible. Furthermore, it can lead to mechanical damage of LIG electrodes [22].

To overcome the challenge of achieving a non-invasive and versatile contact, we present a novel strategy that combines thin-film metallization with laser writing and conversion. This study demonstrates an integrated methodology that enables the electrical connection of graphene-like material without compromising its resistivity. The proposed method using two laser sources is extremely precise and fast, with very low invasiveness. The process is summarized in Figure 1a. A metallic thin film is first deposited onto the polyimide substrate, then some regions are selectively removed through laser ablation to define circuits or contact pads (green laser), and then the exposed substrate is converted into LIG (CO_2 laser).

Direct writing of patterns on substrates offers an incredibly simple way to produce miniaturized supercapacitors, providing the highest degree of design freedom. This is a mature and highly scalable process. However, laser patterning has limitations, mainly due to the maximum achievable laser spot resolution and vertical morphology of LIG structures. In particular, connecting structures with different aspect ratios, like porous LIG and metal thin film, is challenging by using just physical methods. Figure 1d–f show the interface between LIG and a thin film gold, where the connection is visible. In particular, at intermediate magnification (Figure 1e), the typical open, foam-like porous morphology of the LIG can be distinguished. Conversely, at higher magnification (Figure 1f), the carbon structure appears to be multilayered, with the surrounding metallic film remaining comparatively flat and compact. By adjusting the focal plane during FESEM observation, the out-of-plane development of the converted LIG structure was also roughly estimated to be approximately 50 μm. This value is also confirmed by direct optical profilometric measurement (Figure 1c), it confirms the strong three-dimensional development during the conversion. LIG vertical growth and bending, in turn, favor local physical interlocking with the metal-coated substrate, improving the device electrical connection. This fabrication approach is well suited for PCB integration, as it relies exclusively on direct laser writing and PVD. Both are mature, scalable, and alignment-free technologies. Their combination allows rapid customization of electrode geometry and electrical contacts with a high degree of design freedom, enabling symmetric, hybrid, or asymmetric device configurations. Moreover, the physical deposition technique gives us access to a wide range of metals for current collector fabrication or pseudo-electrode realization. In this work, the electrical response was studied by measuring the LIG sheet resistance and, through comparative tests, the gold-LIG contact resistance. Electrochemical tests conducted on a device obtained through the above-described processes showed a cycling stability exceeding 1000 cycles in an acidic environment, Figure 2.

Summarizing, this work aims to validate a fully physical fabrication route for reliable Au-LIG electrical contacts and evaluates its performance in terms of contact resistance, electrochemical stability, and compatibility with scalable manufacturing.

2199160x, 0, Downloaded from https://advanced.onlinelibrary.wiley.com/doi/10.1002/aelm.70576 by Cochraneltalia, Wiley Online Library on [26/10/2026]. See the Terms and Conditions (https://onlinelibrary.wiley.com/terms-and-conditions) on Wiley Online Library for rules of use; OA articles are governed by the applicable Creative Commons License

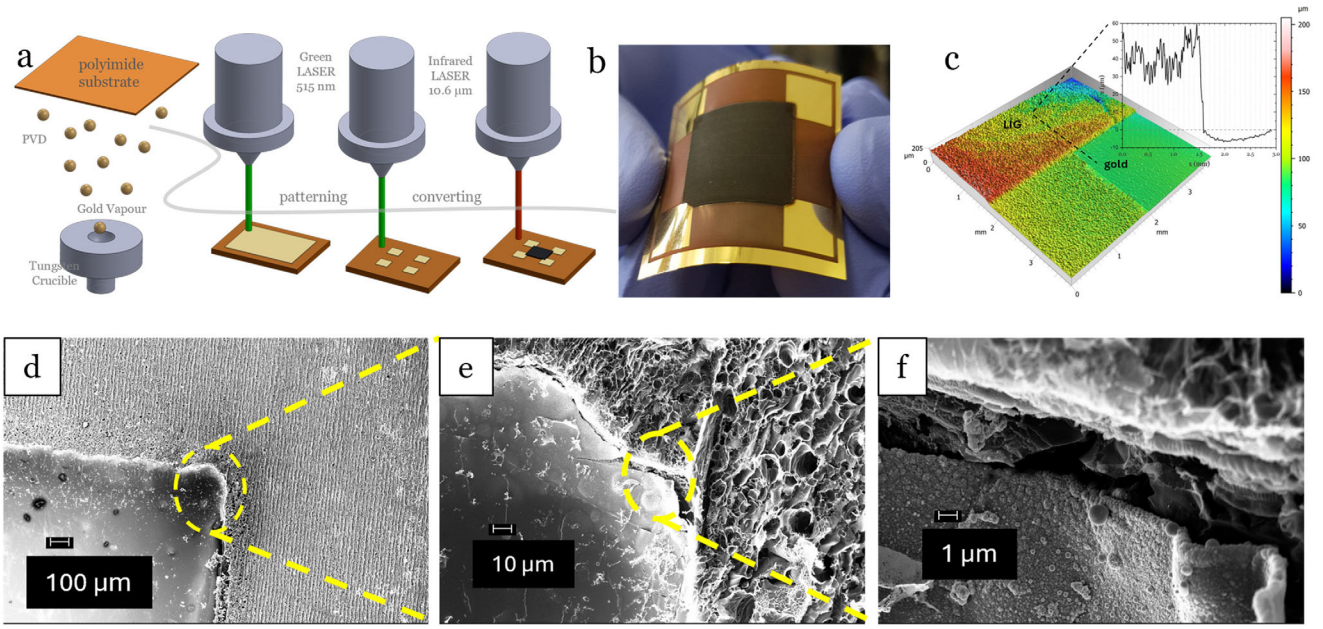

FIGURE 1 | (a) Schematic representation of current collector deposition and substrate LIG conversion, (b) picture of Van Der Pauw 4 pads configuration for sheet resistance evaluation, (c) Measured 3D view with focus variation of the 4-pads sample. The inset cross-section profile gives the elevation of the LIG surface with respect to the gold plane of about 50 µm calculated with the given software, (d-f) FESEM images of Gold-LIG contact under different magnifications.

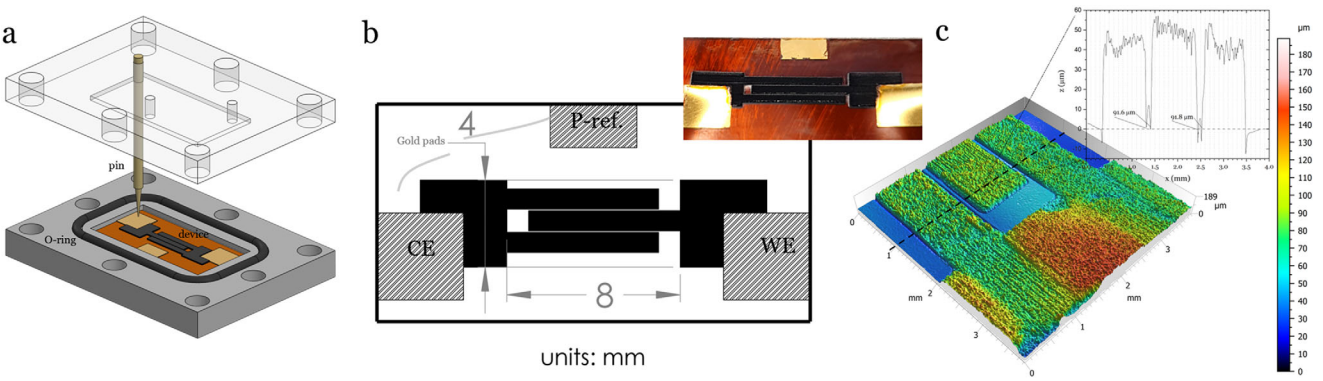

FIGURE 2 | (a) Illustration of the single interdigit device placed in the three-pin setup. (b) Top view of the device geometry. (c) Measured 3D view with focus variation of the interdigitated device. The inset cross-section profile gives the elevation of the LIG surface with respect to the PI plane of about 50 µm, calculated with the given software.

2 | Materials and Methods

2.1 | Electrode Fabrication

The technological processes for the fabrication of electrodes are fully compatible with the microfabrication methods available in the microelectronics and semiconductor industry. In this considered case study, we exploit a 10 cm × 10 cm polyimide substrate, cleaned by 1 h sonication and successively argon plasma treated for 5 min, before any further treatment. The overall fabrication process consists in 3 steps. The first step aims to deposit a high conductive layer over the polyimide substrate. This is done through thermal resistive physical vapor deposition (PVD), which allows to obtain, over the entire substrate, a highly conductive thin metallic film, composed of 10 nm of titanium (that acts as an adhesion layer) and 100 nm of gold (as a conductive layer for the subsequent phases). The deposition was obtained starting from 99.9% purity precursor pellets. After PVD, a green pulsed femtosecond laser (λ_{green} = 515 nm) was used for metallic ablation (second step) to define the circuit paths or pads that will act as current collectors for the active material.

Finally, in the third step, an infrared laser (λ_{IR} = 10.6 µm and maximum nominal output power = 10 W) was used to obtain the conversion of polyimide in graphene-like material. The nominal laser power was set at 30% of the max power with a scan velocity of 50 mm s^{-1}. The writing geometry of the LIG was designed to ensure continuity on the edge and let the laser to scan over the metallic film at the Kapton-metal delimitation. In this way, it is possible to obtain a region where the generated LIG can emerge

2199160x, 0, Downloaded from https://advanced.onlinelibrary.wiley.com/doi/10.1002/aelm.70576 by CochraneItalia, Wiley Online Library on [26/10/2026]. See the Terms and Conditions (https://onlinelibrary.wiley.com/terms-and-conditions) on Wiley Online Library for rules of use; OA articles are governed by the applicable Creative Commons License

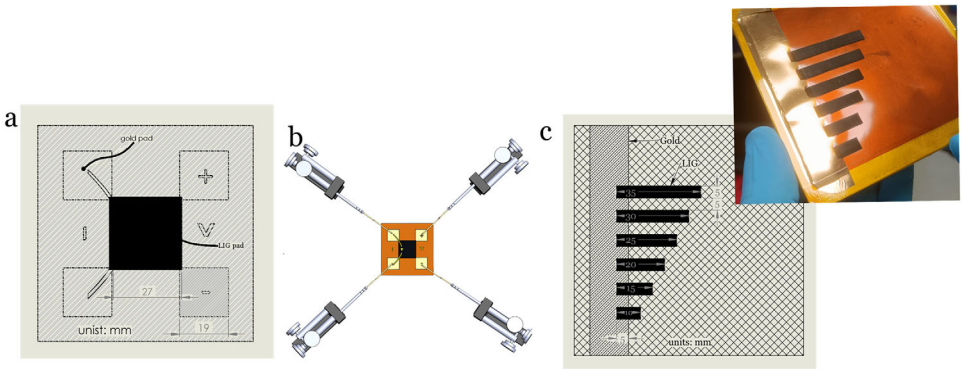

FIGURE 3 | Experimental configurations adopted for the electrical characterization of the fabricated Au-LIG structures. (a) Layout of the sample designed for Van der Pauw measurements, showing the relative positions of the gold contact pads and the LIG active area. (b) Schematic representation of the Van der Pauw measurement setup, where four independent probes are connected to the contact pads to determine the sheet resistance of the conductive layer. (c) Design and optical image of the test structures employed for four-terminal (4T) resistance measurements across the Au-LIG interface. Different overlap lengths between the gold electrodes and the LIG region were investigated to evaluate the electrical contact resistance and the effectiveness of the junction.

vertically around the metallic plane, thereby merging the two substrates and ensuring a good electrical contact.

2.2 | Electrical Characterization

Two types of electrical measurements were carried out to compute the sheet resistance of LIG electrodes and to evaluate the LIG-Au contact resistance. Electrical characterizations were performed using an Agilent 34501 multimeter on 2 different geometries. The first geometry employed a Van der Pauw configuration, Figure 3a to determine the sheet resistance of LIG. The second one Figure 3c, consisted of several strips of different lengths, used to evaluate the contact resistance between gold pads and LIG. The signal was injected and collected with Signatone micromanipulators with copper tips.

2.3 | Electrochemical Characterization

Measurements were made using VMP3 Biologic potentiostat in a three-electrode custom cell, with soft-touch contact pins. The cell was sealed by an o-ring. The measurements were carried out to confirm the robustness of the electrical contact in a typical operating condition. The adopted electrochemical setup is shown in Figure 2: the tested device was characterized by an acidic electrolyte (0.5 M H_2SO_4), a working electrode, a counter electrode, and a pseudo-reference electrode.

2.4 | Evaluation Formulas

The sheet resistance was calculated through the Van der Pauw formula:

$$Rs = \frac{\pi R_v}{\ln 2} \tag{1}$$

$$e^{-\pi R_v/R_s} + e^{-\pi R_h/R_s} = 1 \tag{2}$$

where $R_v = R_{vertical}$, and $R_h = R_{horizontal}$, are the resistances taken in the two directions on the Van der Pauw geometry.

The capacitance of the single electrode (C) and capacitance density C_A can be estimated by CV curves using the following equations:

$$C = \frac{1}{V_w} \cdot \int I_d dt \tag{3}$$

where V_w is the voltage window and I_d the discharge current. Only the discharging part was taken into account. The capacitance per unit area (C_a) was calculated by the following:

$$C_A = \frac{1}{A_g \cdot V_w} \cdot \int I_d dt \tag{4}$$

where the term A_g represents the geometrical area of the sample, namely the area exposed to the electrolyte (the gap between the fingers of the electrodes is included). The energy (E_d) and power density (P_d) performance of the device were calculated using the following formulas:

$$P_d = \frac{1}{A_g \cdot t_d} \int V_d I_d dt \tag{5}$$

$$E_d = \frac{1}{A_g} \int V_d I_d dt \tag{6}$$

(Capacitance 23 mF cm^{-2}, Power 8 μW cm^{-2}, Energy 1.6 μWh cm^{-2})

2.5 | Physical Characterization

Different physical characterization techniques were used: the topographies were performed by 3D focus variation optical microscope, model Bruker Alicona InfiniteFocus G6. The reconstructed topographies were processed by using the metrological software

2199160x, 0, Downloaded from https://advanced.onlinelibrary.wiley.com/doi/10.1002/aelm.70576 by CochraneItalia, Wiley Online Library on [26/10/2026]. See the Terms and Conditions (https://onlinelibrary.wiley.com/terms-and-conditions) on Wiley Online Library for rules of use; OA articles are governed by the applicable Creative Commons License

TABLE 1 | Typical metals deposited via PVD adequate for hybrid electrochemical systems.

Material	Melting Point°C	Vap. Temp. @10^{-8} mBar°C	Deposition technique	Ref.
Mn	1244	507	T, S, e-Beam	[25]
Au	1064	807	T, S, e-Beam	
Ti	1660	1067	Thermal	
Ru	2300	1780	Thermal	
V	1890	1162	T, S, e-Beam	
Cu	1083	727	T, S, e-Beam	

Mountains Map v11. This technology allows to reconstruct the 3D surface of a multi-material sample without contact, with high resolution. Topographies were performed using a 4× objective 30 mm working distance. Field Emission Scanning Electron Microscopy (**FESEM**) to investigate the morphology, **Raman** spectroscopy to evaluate the structure and the disorder level of the LIG generated, and Energy Dispersive Spectroscopy (**EDX**) to assess the presence of metallic contact below the generated LIG active material. Raman spectroscopy was performed with a Virsa Raman Analyser from Renishaw. Parameters used were 532 nm Laser, 3 mW, 10 s of exposure, and 5 accumulations. The topological observation was conducted via a Zeiss Supra 40 FESEM. InLens detector images at low electron beam energy (5 keV) and an aperture size 30 μm allows to examine the top-view morphology and porosity of the converted structures and to confirm the graphene-like nature and quality of the soldering. The **SEM-EDX** mapping elemental maps were produced using a high accelerating voltage (15 kV).

3 | Results and Discussion

This study aims to overcome a major challenge in the functional integration of LIG in various multi-material environments. In particular, obtaining reliable and standardized electrical contacts of LIG remains an issue. This technological gap can be overcome by treating the substrate/precursor (PI) prior to LIG formation, enabling the integration of high-purity metallic contacts by using a fully dry physical deposition technique. This approach represents a significant improvement not only for planar electronic applications, but also for any field requiring standardized and scalable electric contacts. Furthermore, the implantation of pads facilitates PCB board integration. The adoption of metal deposition techniques also allows full versatility in the fabrication of hybrid micro-supercapacitors, allowing the electrodes to be processed with different materials [23, 24]; in particular, the deposited metals can be oxidized to obtain fully customizable hybrid devices. Thermal evaporation PVD was selected due to its higher scalability and deposition rates compared to magnetron sputtering, its absence of droplet formation issues (typical of Arc-PVD), and its suitability for deposition on flat substrates where line-of-sight constraints do not limit film uniformity. Table 1 reports typical materials that can be used.

Compared to other wet metallization methods, the physical deposition technique provides precise control over both geometry (through masking) and vertical architecture (through precise control of thin film thickness). Furthermore, high vacuum ensures the quality and purity of the precursors. After Ti-Au layer deposition on the PI substrate, it is possible to selectively remove the metal film using a femtosecond laser while leaving the underlying polymer essentially unchanged. This selectivity arises from the very different behavior exhibited by metals and polymers when irradiated with a green femto-second laser [26]. In metals, such as gold, ablation can also occur at relatively low fluence by exploiting photomechanical effects. In fact, when irradiated by a femtosecond laser pulse, the free electrons in the metal strongly absorb the optical energy and reach very high effective temperatures on a timescale much shorter than electron-phonon coupling. As a result, the energy remains initially confined within the electronic subsystem, while the lattice stays comparatively cold during the laser pulse. The subsequent energy transfer from electrons to the lattice can drive material removal through different non-equilibrium mechanisms such as stress-driven ejection or rapid phase instability. In contrast, polymer absorption (like PI) is much weaker at green wavelengths. Moreover, PI is not characterized by a free electron system, significantly increasing the damage threshold with respect to metals. Therefore, by working above the gold threshold and below the PI one, the Ti-Au layer can be removed while the polymer substrate remains essentially unmodified [27]. After the selective removal of the metal layer, carbon electrodes can be fabricated by locally inducing the graphitization of the PI substrate. This is achieved by exploiting the strongly different response of the materials to infrared radiation. While PI efficiently absorbs IR radiation of a CO_2 laser and it is thermally converted into LIG [28], gold largely reflects radiation in this spectral range [29, 30] and therefore remains essentially unaffected during the laser processing. As a result, the CO_2 laser selectively converts the exposed polyimide into conductive carbon without directly ablating the gold tracks. As a consequence, the laser conversion of polyimide into LIG close to the gold layer creates a rectangular overlap region between the LIG and the gold electrodes, enabling physical and electrical contact through local graphitization and interfacial soldering. In order to better understand the material arrangement at the interface, EDX maps were performed using a 15 keV electron beam to induce the production of K lines for titanium and carbon, and M lines for gold. Information concerning the EDX maps is reported in the Supporting Information. After laser processing, it is possible to identify the K-alpha titanium, K-alpha carbon, and M-alpha gold signals. In particular, the EDX maps reveal the elemental distribution at the LIG-metal interface and, owing to the porous nature of LIG, it is possible to carry out analyses below the LIG surface.

2199160x, 0, Downloaded from https://advanced.onlinelibrary.wiley.com/doi/10.1002/aelm.70576 by Cochraneltalia, Wiley Online Library on [26/10/2026]. See the Terms and Conditions (https://onlinelibrary.wiley.com/terms-and-conditions) on Wiley Online Library for rules of use; OA articles are governed by the applicable Creative Commons License

The maps suggest that the formation of the overlap region is governed by two distinct mechanisms. First, the CO_2 laser beam directly irradiates and converts the PI region immediately adjacent to the gold edge, which remains accessible to infrared radiation. Second, the high thermal load generated during PI-to-LIG conversion propagates laterally via thermal conduction into the PI underlying the gold edge, resulting in localized graphitization in the contact region. Furthermore, the gold layer in the overlap region undergoes a significant structural change. The thermal load associated with LIG conversion causes the gold film to lose structural cohesion. According to Wang et al. [20], the local conversion temperature during LIG formation ranges between 1000°C and 2000°C. Although the metallic film is exposed to only a fraction of this thermal load, the resulting thermal stress leads to deformation of the gold film and promotes its inter-locking with the porous carbon matrix. The Ti layer works primarily as an adhesive layer between the Au film and the PI substrate; in fact, its role is well known in thin film technology, ensuring superior mechanical stability to the metal-polymer structure. The electrical contact is therefore established primarily through the Au-LIG interface, with titanium acting exclusively as a mechanical anchor for the gold film to the PI substrate. As regards its role in electrical conductivity at the contact zone, we can assume that titanium does not have a significant effect on this aspect.

The **sheet resistance** (SR) of the produced LIG was obtained as a preliminary measurement. As widely reported, LIG sheet resistance is strongly related to the power of the laser sources employed for the conversion [31]. Measurements were performed using the Van der Pauw technique (Figure 3a), which allows to determine the sheet resistance. A value of SR = 16.7 Ω/□ was obtained, consistent with values reported by Chen et al. [31] and for similar laser conditions [32].

In Figure 3c is possible to notice a second geometry used to evaluate the Au-LIG electrical contact resistance. First, a rectangular gold layer was deposited on the polyimide substrate; subsequently, LIG stripes of different lengths were generated in contact with the metal pad. For each line, the total resistance was measured as a function of the LIG track length. Since the resistance of the LIG scales linearly with length, the measured resistance (R_{tot}) can be expressed as the sum of the LIG track resistance ($R_{LIG}(L)$), the Au-LIG contact resistance (R_{cont}), and the resistance of the gold part (R_{Au}).

$$R_{tot} = R_{Au} + R_{cont} + R_{LIG}(L)$$

By plotting the total resistance as a function of the LIG length and fitting the data with a linear regression (Figure 4), the intercept of the fit provides $R_{tot}(L = 0) = R_{Au} + R_{cont}$. Because $R_{Au} \approx 0.3$ Ω/□ is negligible given the high conductivity of the gold film compared to the LIG resistance, we can affirm that the intercept gives us the contact resistance (R_{tot} (L = 0) ≈ R_{cont}). Data show that such contact resistance ranges from approximately 7.6 Ω in the least favorable case down to almost 1.3 Ω in the best-performing case. These results demonstrate that the Au-LIG contact obtained during the laser conversion process provides a low-resistance electrical interface, representing an important improvement for the fabrication of flexible electronic devices.

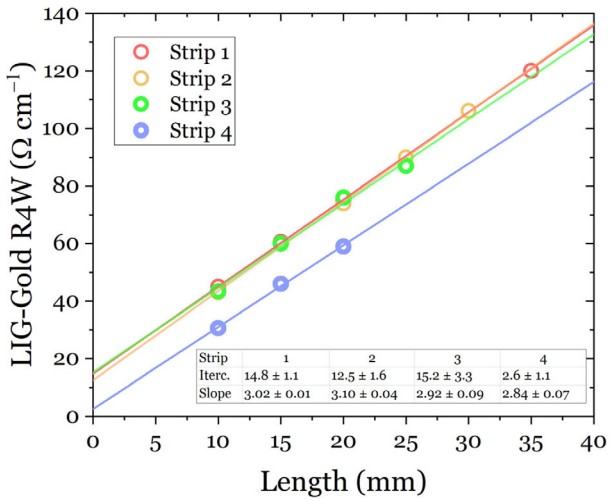

FIGURE 4 | Four-terminal resistance measurements of LIG across the gold contact, normalized with respect to the stripe width for different lengths as depicted in Figure 3c.

In Figure 5 is possible to notice the Raman analysis of different carbon paths. The purpose of this analysis is not to optimize the laser-processing parameters, but rather to evaluate how small variations around the selected fabrication conditions (p = 30%, f = 1kHz, v = 50 mms^{-1}) affect the structural characteristics of the LIG. The typical Raman spectrum of carbon-based samples shows two main bands in the first-order range (Figure 6a) in which we find **D**-band peak (1350 cm^{-1}, present only in the defected carbon samples) and **G**-band peak (1585 cm^{-1}, present both in ordered and disordered carbon-based samples, related to in-plane E2g stretching mode of sp_2 carbon structure). According to Liu X. et al. [33], the capacitance of a supercapacitive carbon-based electrode and its Raman evaluated order degree are correlated. In particular, carbon-based electrodes showing higher disorder can generally also provide higher capacitances. Following the same approach, we decided to focus on the full width at half maximum of D band (FWHM D, proportional to the domain size distribution and with capacitance) and on I_D/I_G ratio (directly proportional to the in-plane size of graphene-like domains). Therefore, following this interpretation, highly capacitive LIG is characterized by high FWHM of D and low I_D/I_G ratio. From the absolute intensity ratios and the relative ratios between the peaks shown in (Figure 5), we can see how the analysis allows us to infer the direction in which the surface capacitance is developing as a function of an operative point that is affect by changes in illumination parameters, that are power fraction **p**, frequency **f**, and scan velocity **v** [34].

However, it must be underlined that Raman detects structural disorder regardless of the accessibility by the electrolyte. This means that, in the hypothetical case of low pore accessibility to an electrolyte but high structural disorder, the resulting capacitance will not fully exploit this advantage. To investigate how these parameters change the quality of the LIG, we decided to prepare 3 matrices, in which 2 parameters are varied, fixing the third and evaluating the FWHM D and I_D/I_G. Graphs presented in Figure 6 can give a hint on the hierarchy in the LIG conversion. Percentage of the power, in the considered range (28% – 32%) is the less affecting parameter, since both in [v vs %] and [f vs %] it does

2199160x, 0, Downloaded from https://advanced.onlinelibrary.wiley.com/doi/10.1002/aelm.70576 by CochraneItalia, Wiley Online Library on [26/10/2026]. See the Terms and Conditions (https://onlinelibrary.wiley.com/terms-and-conditions) on Wiley Online Library for rules of use; OA articles are governed by the applicable Creative Commons License

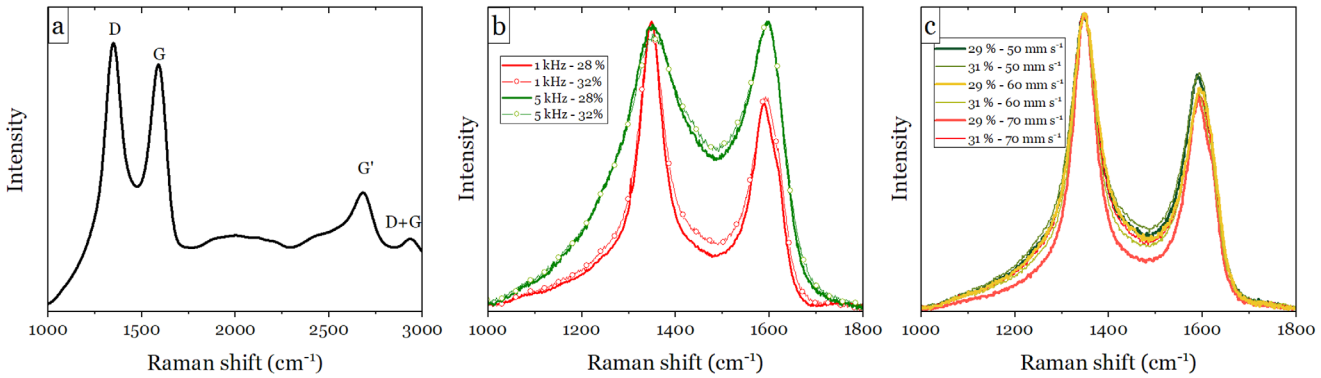

FIGURE 5 | Raman spectra of LIG generated through different illumination conditions.

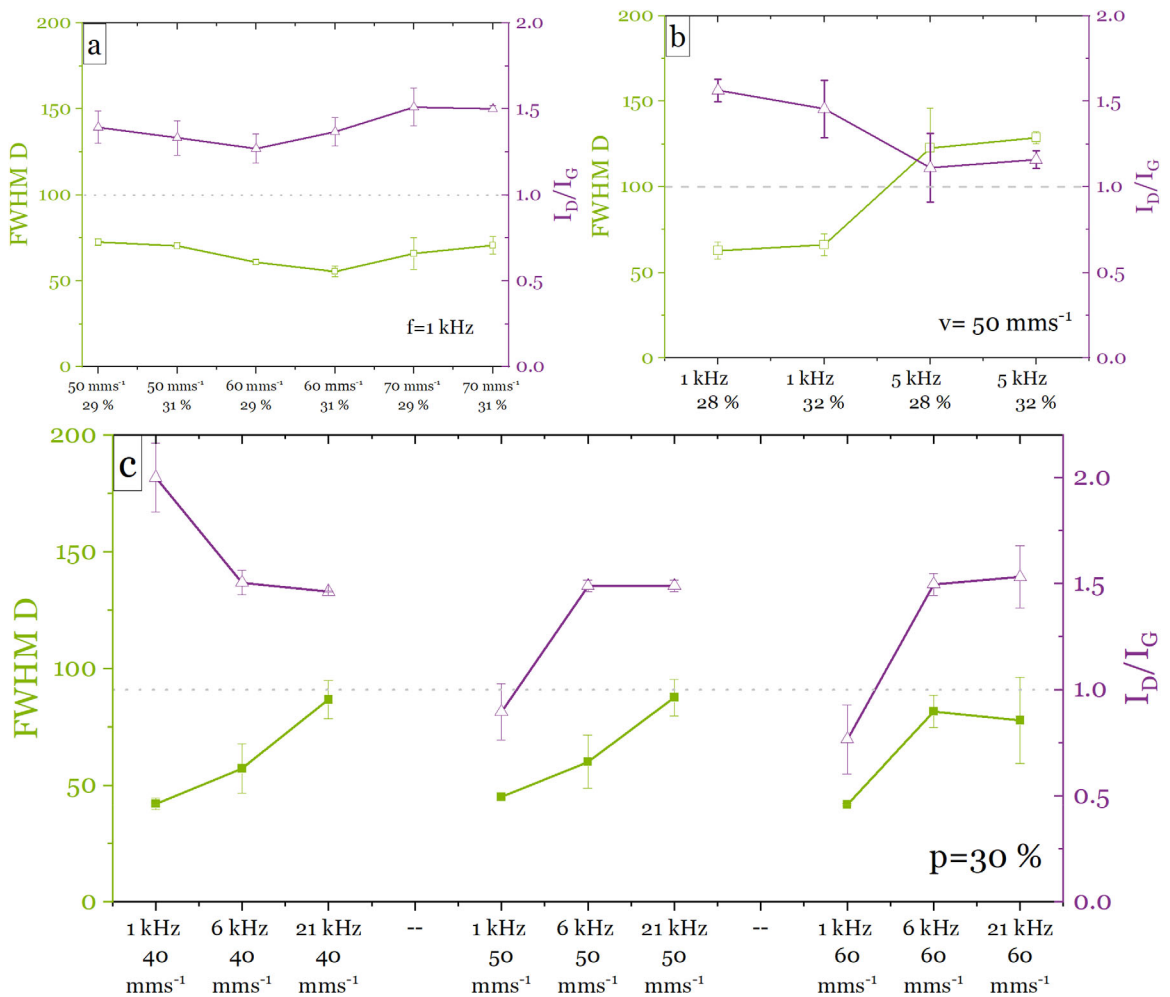

FIGURE 6 | Comparatative for domain and disorder ratio around the LASER parameters chosen for soldering the two materials. (a) Comparative plot of FWHM D peak and I_D/I_G fixing frequency at 1 kHz and varying power and scribing scan speed. (b) Comparative plot of FWHM of D peak and I_D/I_G ratio fixing scribing scan speed at 50 mm s^{-1} while varying power and pulsing frequency. (c) Comparative plot of FWHM and I_D/I_G ratio fixing power source while varying scribing scan speed and pulsing frequency.

not produce any significant effect (Figure 6a,b), while increasing velocity appears to show a slight trend toward higher I_D/I_G ratio about 2 (meaning higher dimensions of in-plane size of graphene-like domains [34]) (Figure 6a). A key role parameter is instead played by the illumination frequency, which seems to be directly proportional to the disorder degree. In particular, considering [f vs %], moving from 1 to 5 kHz leads to a general broadening of the D and G bands and a reduction in the I_D/I_G ratio, suggesting a reduction in graphene-like size and an increase in the domain size distribution. Overall, within the investigated parameter range,

2199160x, 0, Downloaded from https://advanced.onlinelibrary.wiley.com/doi/10.1002/aelm.70576 by CochraneItalia, Wiley Online Library on [26/10/2026]. See the Terms and Conditions (https://onlinelibrary.wiley.com/terms-and-conditions) on Wiley Online Library for rules of use; OA articles are governed by the applicable Creative Commons License

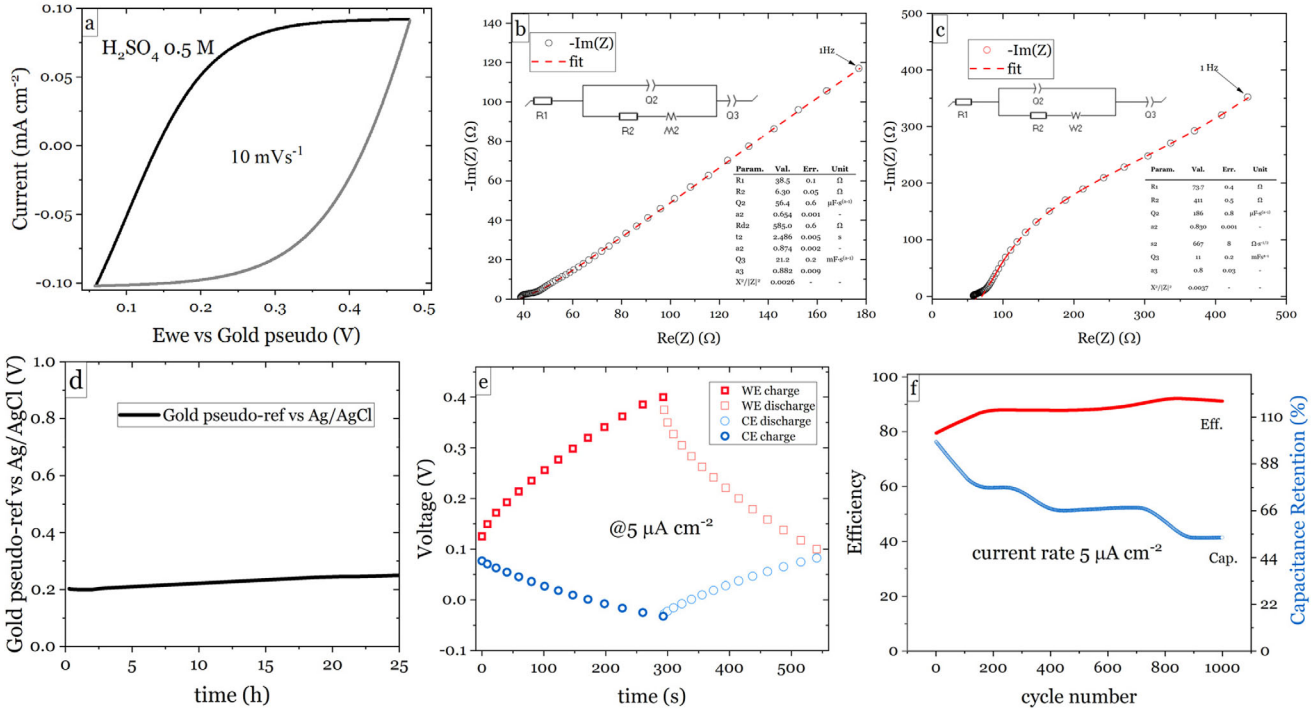

FIGURE 7 | (a) CV curve for the device in an acid electrolyte. At a scan rate of 10 mVs^{-1}. (b-c) PEIS curve of the electrode before and after cycling. (d) Monitoring Gold pseudo-electrode voltage drift while cycling. (e) CCCD curves of the device at a current density of 5 μA cm^{-2}. (f) Capacitance retention of the device at a current density of 5 μA cm^{-2} of 1000 cycles.

[f vs v] plot (Figure 6c) suggests that the laser frequency is the predominant parameter governing the structural evolution of LIG. Increasing the frequency systematically broadens the D band, indicating an increase in structural disorder. In contrast, the influence of the scanning velocity appears limited, producing an appreciable variation of the I_D/I_G ratio only at 1 kHz, while at higher frequencies the values remain comparable for all the studied velocities. At the highest investigated velocity (60 mm s^{-1}), both the I_D/I_G ratio and the D band FWHM increase significantly when moving from 1 kHz to 6 kHz, but further increasing the frequency does not produce substantial additional changes, as both parameters tend to stabilize, suggesting the system reaches a saturation regime.

3.1 | Electrochemical Measurements

The full set of electrochemical characterizations is reported in Figure 7. The cyclic voltammetry in Figure 7a clearly reinforces the predominantly electrostatic nature of the charge storage mechanism in the LIG electrodes. The boxed shape of the voltammogram, combined with the absence of discernible redox peaks, confirms the pure EDLC response. The slight deviation from ideal rectangular symmetry, particularly at low scan rate, is consistent with the resistive limitations previously described and can be attributed to intrinsic sheet resistance together with the contribution of the gold-LIG contact interface. Nonetheless, the high repeatability within the potential window indicates excellent chemical stability of the LIG surface under acidic conditions. Figure 7b presents the Nyquist plots obtained before and after cycling. As anticipated, the high-frequency intercept provides direct information on the equivalent series resistance, and the observed value 39 Ω is fully consistent with the expected contribution from the current collector-electrode contacts, electrode, and the electrolyte pathway. After 1000 cycles, the slope of the impedance curve becomes progressively less vertical, suggesting an increase in Warburg-type behavior. This indicates the onset of diffusion-related limitations and possible surface degradation. The enlargement of the semicircular region after cycling highlights a rise in charge-transfer resistance, which is likely associated with gradual surface passivation or partial loss of accessible electrochemical area. These changes collectively suggest that although the device remains functional, efficiency and ion accessibility are moderately compromised after long term operation.

The EIS plots were fitted using an equivalent circuit consisting of a series resistance (R1), followed by a parallel combination of a constant phase element (Q2) and a branch composed of a resistance (R2) and a finite-length Warburg element (W2). An additional constant phase element (Q3) was included to reproduce the low-frequency capacitive response. The relatively low value of R2 (6.3 Ω) indicates efficient charge transport within the electrode, whereas the high contribution of the Warburg element reveals that ion diffusion inside the porous LIG network plays a significant role in determining the overall impedance response. The non-ideal behavior of Q2 (a2 = 0.654) reflects the structural heterogeneity of the laser-induced graphene, while Q3 (a3 = 0.882) approaches an ideal capacitive response, describing the global charge-storage behavior of the electrode at low frequencies. Compared with the pristine EIS, the device after 1000 cycles exhibited significantly higher resistance values. In particular, the increase of both R1 and R2 suggests that the observed impedance changes cannot be solely attributed to modifications

2199160x, 0, Downloaded from https://advanced.onlinelibrary.wiley.com/doi/10.1002/aelm.70576 by CochraneItalia, Wiley Online Library on [26/10/2026]. See the Terms and Conditions (https://onlinelibrary.wiley.com/terms-and-conditions) on Wiley Online Library for rules of use; OA articles are governed by the applicable Creative Commons License

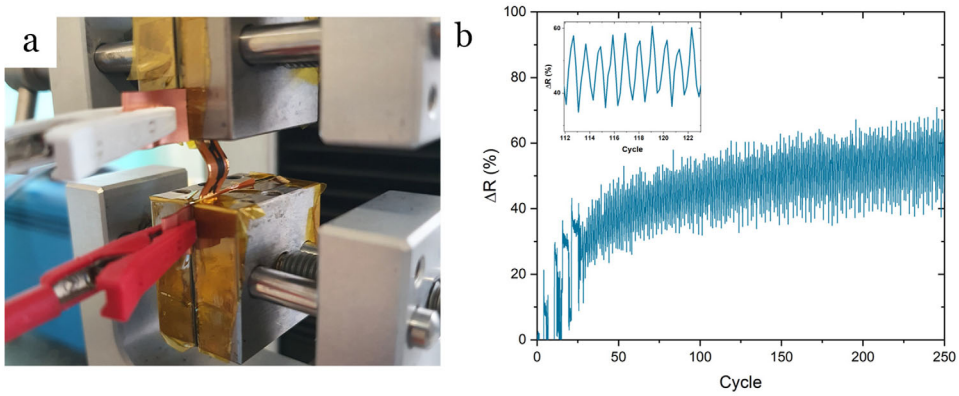

FIGURE 8 | (a) Set-up adopted for the electromechanical bending characterization of the Au-LIG device. The sample was bent to an angle of approximately 130° (sagitta ≈ 5 mm) while maintaining electrical connections through insulated clamps, enabling continuous monitoring of the device resistance under severe flexural deformation. (b) Relative resistance variation (ΔR/R0) of the Au-LIG device during 250 bending cycles. The electrical response exhibits a progressive increase in resistance during the initial cycles, followed by a gradual stabilization. The inset shows a magnified view of consecutive cycles, highlighting the repeatability of the electromechanical response.

within the LIG porous network. A most favorable explanation is the progressive degradation of the external electrical contacts. Since the gold pads were connected using Cu-Sn (alloy pins), capillary penetration of the acidic electrolyte may have promoted corrosion phenomena at the pad interface during prolonged electrochemical cycling. Such degradation would introduce additional resistive contributions and non-ideal interfacial effects, thereby altering the fitted circuit parameters. The stability of the gold pseudo-reference electrode is examined in Figure 7d. The slow and monotonic drift of the potential versus Ag/AgCl reference electrode, remaining confined within a narrow range of a few tens of millivolts over 24 h demonstrates that the gold contact maintains a sufficiently stable potential to be used as a pseudo-reference in this configuration. The absence of abrupt fluctuations indicates that the acidic environment does not promote rapid corrosion or instability of the gold surface. This supports the reliability of the reference point used during the CV and galvanostatic measurements. Figure 8d shows the galvanostatic charge/discharge behavior at a current density of 5 μA cm^{-2}. Both the working electrode (WE) and counter electrode (CE) display nearly linear potential variation during charging and discharging, which is characteristic of capacitive systems. The slight asymmetry between charge and discharge slopes points again to resistive contributions and interfacial polarization effects. The voltage profiles remain smooth and continuous, implying that no faradaic side reactions or instabilities interfere significantly during cycling within the chosen potential window. Finally, Figure 8e summarizes the cycling performance at the same current density. The coulombic efficiency remains remarkably high throughout all 1000 cycles, stabilizing above 90%, which confirms limited parasitic reactions and high reversibility of the charge/discharge process. Conversely, the areal capacitance retention shows a gradual decrease, leveling around 12%–15% of the initial value after extended cycling. This decline aligns with the impedance findings and indicates that after prolonged operation, ion accessibility to the porous LIG network becomes increasingly limited. Possible causes include partial detachment of surface fragments or progressive occlusion of pores by trapped ions. Despite this reduction, the device maintains consistent operational behavior without failure, confirming that the LIG structure retains its mechanical integrity even under acidic conditions. Overall, the combined electrochemical analyses highlight both the robustness and the limitations of planar LIG electrodes in acidic media. While the device preserves high reversibility and stable potential reference behavior, long-term cycling induces moderate increases in series and charge-transfer resistance, along with a noticeable yet predictable decrease in capacitance. These findings confirm the initial design considerations and point to clear directions for optimization, particularly in reducing sheet and contact resistance and improving structural resilience of the active surface during extended electrochemical cycling. Device specifications:

- Sheet resistance LIG 16.65 Ω/□
- Contact resistance Au-LIG: 2.6 Ω cm^{-1}
- Device geometric area 0.48 cm^{-2}
- Device capacitance density (max) 23 mF cm^{-2}
- Device geometrical ratio WE/CE 1:2
- Device power density 8 μW cm^{-2}
- Device energy density 1.6 μWh cm^{-2}
- Electrolyte H_2SO_4 0.5 M, pH = 0.3

To further validate the robustness of the Au-LIG electrical contact under mechanical deformation, bending cycling tests were performed on the fabricated device. Bending trials were conducted using a universal testing machine (FZ3-X500, Test Engineering) equipped with a load cell of 500 N.

Figure 8 shows the experimental setup used for the electromechanical bending tests. The device was electrically connected through a copper band compressed between insulated clamps and subjected to a controlled bending deformation. During the test, the sample was bent to an approximate bending angle of 130°, corresponding to a sagitta of about 4 mm over a span of approximately 15 mm, while the electrical response was continuously monitored. The normalized resistance variation

2199160x, 0, Downloaded from https://advanced.onlinelibrary.wiley.com/doi/10.1002/aelm.70576 by CochraneItalia, Wiley Online Library on [26/10/2026]. See the Terms and Conditions (https://onlinelibrary.wiley.com/terms-and-conditions) on Wiley Online Library for rules of use; OA articles are governed by the applicable Creative Commons License

ΔR (%) was recorded continuously over 250 bending cycles, and the results are reported in Figure 8b. The plot shows a clear periodic modulation of the resistance, consistent with the reversible piezoresistive response of LIG under repeated mechanical deformation, a behavior already well established in the literature for LIG-based strain sensors [33]. Each oscillation corresponds to a complete bend-unbend cycle, and the periodic nature of the signal confirms that the Au-LIG contact remains electrically continuous throughout the entire test.

Two distinct regimes can be identified. In the first approximately 50 cycles, the resistance baseline progressively shifts upward. This transient behavior is attributed to the irreversible formation and propagation of microcracks within the LIG structure during the initial bending cycles, which partially hinder charge transport and cause the shift of the baseline. This phenomenon is well known for LIG and porous carbon structures on flexible substrates and does not involve failure of the metal-LIG interface itself [35]. After this initial phase, the device reaches a stable regime in which the resistance oscillates reproducibly between approximately 35% and 65% ΔR, with no divergence or progressive drift observed up to 250 cycles. It is possible to avoid the initial transient by transferring the device onto a PDMS substrate, as demonstrated in previous work [36]. However, this strategy falls outside the scope of the present work, whose focus is the electrical and electrochemical characterization of the Au-LIG contact in its planar configuration. Overall, these results demonstrate that the Au-LIG contacts fabricated through the proposed fully physical route maintain their electrical integrity under repeated mechanical deformation, supporting the claim of robust and metal-LIG bonding on flexible polyimide substrates.

4 | Conclusion

In this work, we have demonstrated that a fully physical and dry fabrication method can be used to integrate, into a single device, two materials with different conductivity and structure, namely metal and a carbon-based soft material. By shaping the metal contacts prior to LIG formation and subsequently creating the active material soldered with current collector leads to a robust and reproducible electrical connection without the need for wet chemistry or photolithographic processes. The defined fabrication technique allows us to overcome one of the main limitations of LIG technology, namely the formation of low-resistance and scalable electrical contacts. The resulting minimal electrical contact resistance is 2.6 Ω cm^{-1}, which is certainly a relevant and very promising value for microscale electronic devices. The adopted laser processes enable complete scalable manufacturing and provide high geometric freedom for micro-soft electronics. Summarizing, femtosecond laser patterning enables selective removal of metallic layers with sub-micrometer precision, while CO_2 laser graphitization allows localized conversion of polyimide into conductive LIG. This dual-wavelength strategy provides the possibility to realize complex planar geometries while preserving compatibility with large-area processing and possible integration into roll-to-roll systems, with possible applications range from low aspect ratio electronics to more advanced sensing [1, 38]. The prosecution of this study involves an encapsulation strategy for the electrolyte, parametrization of the metal thickness layer with sputter deposition techniques, and optimal integration of a pseudo-reference for advanced sensing.

Acknowledgements

- This result is part of a project that has received funding from the European Research Council (ERC) under the European Union's ERC Starting Grant agreement "CO2CAP" No. 949916. This manuscript reflects only the authors' views and opinions, neither the European Union nor the European Commission can be considered responsible for them.
- This work was conducted within the Technologies for Sustainability Flagship of the Istituto Italiano di Tecnologia.
- This article was partially funded under the National Recovery and Resilience Plan (NRRP), Mission 4 "Education and Research"—Component 2 "From research to business"—Investment 3.1 "Fund for the realization of an integrated system of research and innovation infrastructures"—Call for tender No. n. 3264 of 28/12/2021 of Italian Ministry of Research funded by the European Union—NextGenerationEU—Project code: IR0000027, Concession Decree No. 128 of 21/06/2022 adopted by the Italian Ministry of Research, CUP: B33C22000710006, Project title: iENTRANCE.

Open access publishing facilitated by Politecnico di Torino, as part of the Wiley - CRUI-CARE agreement.

Conflicts of Interest

The authors declare no conflicts of interest.

Data Availability Statement

The data that support the findings of this study are available from the corresponding author upon reasonable request.

References

1. H. Yu, J. Bian, F. Chen, J. Ji, and Y. Huang, "Ultrathin, Graphene-in-Polyimide Strain Sensor via Laser-Induced Interfacial Ablation of Polyimide," *Advanced Electronic Materials* 9, no. 9 (2023): 2201086, https://doi.org/10.1002/aelm.202201086.

2. D. Arcoraci, P. Zaccagnini, M. Castellino, et al., "Enhancing the Performance and Mechanical Stability of 2D-Based Hybrid Micro-Supercapacitors Using Dendritic-Gold as Framework Layer," *Electrochimica Acta* 453 (2023): 142346, https://doi.org/10.1016/j.electacta.2023.142346.

3. A. Kaidarova and J. Kosel, "Physical Sensors Based on Laser-Induced Graphene: A Review," *IEEE Sensors Journal* 21, no. 11 (2021): 12426–12443, https://doi.org/10.1109/JSEN.2020.3034845.

4. S. Zhang, A. Chhetry, and M. A. Zahed, "On-Skin Ultrathin and Stretchable Multifunctional Sensor for Smart Healthcare Wearables," *npj Flexible Electronics* 6 (2022), 11, https://doi.org/10.1038/s41528-022-00140-4.

5. G. Nadalini, A. Dallinger, D. Sottocorno, F. Greco, F. Borghi, and P. Milani, "Soft Electronic Switches and Adaptive Logic Gates Based on Nanostructured Gold Networks," *Advanced Electronic Materials* 11, no. 7 (2025): 2400717, https://doi.org/10.1002/aelm.202400717.

6. Y. Houeix, D. Gerardo, F. J. Romero, et al., "Dry Laser-Induced Graphene Fractal-like ECG Electrodes," *Advanced Electronic Materials* 10, no. 7 (2024): 2300767, https://doi.org/10.1002/aelm.202300767.

7. H. Tetik, E. Markgraf, K. Kato, V. N. Chan, and M. H. Malakooti, "Highly conductive laser-induced graphene through the deposition of liquid metal particles for flexible electronics," *Flexible and Printed Electronics* 8, no. 3 (2023): 035001, https://doi.org/10.1088/2058-8585/ace26b.

2199160x, 0, Downloaded from https://advanced.onlinelibrary.wiley.com/doi/10.1002/aelm.70576 by CochraneItalia, Wiley Online Library on [26/10/2026]. See the Terms and Conditions (https://onlinelibrary.wiley.com/terms-and-conditions) on Wiley Online Library for rules of use; OA articles are governed by the applicable Creative Commons License

8. A. Salvia, A. Mostaccio, G. Antonelli, E. Martinelli, and G. Marrocco, "Full-LIG Wireless Batteryless Sensor for the Detection of Amines," in *2023 IEEE International Conference on Flexible and Printable Sensors and Systems (FLEPS)* (IEEE, 2023), 1–4, https://doi.org/10.1109/FLEPS57599.2023.10220350.

9. M. G. Stanford, J. T. Li, Y. Chyan, Z. Wang, W. Wang, and J. M. Tour, "Laser-Induced Graphene Triboelectric Nanogenerators," *ACS Nano* 13, no. 6 (2019): 7166–7174, https://doi.org/10.1021/acsnano.9b02596.

10. J. Lin, Z. Peng, Y. Liu, et al., "Laser-Induced Porous Graphene Films From Commercial Polymers," *Nature Communications* 5, no. 1 (2014): 5714, https://doi.org/10.1038/ncomms6714.

11. J. Bin In, B. Hsia, J. H. Yoo, et al., "Facile Fabrication of flexible All Solid-State Micro-Supercapacitor by Direct Laser Writing of Porous Carbon in Polyimide," *Carbon (New York)* 83 (2015): 144–151, https://doi.org/10.1016/j.carbon.2014.11.017.

12. A. Lamberti, F. Clerici, M. Fontana, and L. Scaltrito, "A Highly Stretchable Supercapacitor Using Laser-Induced Graphene Electrodes onto Elastomeric Substrate," *Advanced Energy Materials* 6, no. 10 (2016): 1600050, https://doi.org/10.1002/aenm.201600050.

13. R. Miyakoshi, S. Hayashi, and M. Terakawa, "Direct Patterning of Conductive Structures on Hydrogels by Laser-Based Graphitization for Supercapacitor Fabrication," *Advanced Electronic Materials* 9, no. 5 (2023): 2201277, https://doi.org/10.1002/aelm.202201277.

14. S. P. Lee, P. S. Chee, C. H. Tan, K. F. Chong, E. H. Lim, and C. Guan, "A Review on Laser-Induced Graphene in Flexible Energy Storage: From Materials Selection to Biomedical Applications," *Chemical Engineering Journal* 499 (2024): 156110, https://doi.org/10.1016/j.cej.2024.156110.

15. M. Liu, J.-C. Liu, Y. Zhang, et al., "Current Collectors for Supercapacitors: Objectives, Modification Methods and Challenges," *ChemElectroChem* 12, no. 1 (2025): 2400513, https://doi.org/10.1002/celc.202400513.

16. M. Saito, S. Harada, R. Imai, K. Son, and T. Fujie, "Flexible Thin-Film Heater Composed of Laser-Induced Graphene and Poly(D, L-Lactic Acid) with Electro- and Photo-Thermal Properties toward Cancer Thermotherapy," *Advanced Electronic Materials* 12 (2025): 2500062, https://doi.org/10.1002/aelm.202500062.

17. W. Babatain, C. Park, H. Ishii, and N. Gershenfeld, "Laser-Enabled Fabrication of Flexible Printed Electronics with Integrated Functional Devices," *Advanced Science* 12 (2025): 2415272, https://doi.org/10.1002/advs.202415272.

18. M.-H. Seo, "Mechanically Robust and Highly Conductive Laser-Induced Graphene-Metal Heterojunction for High-Performance Flexible Sensors," *Soft Mechatronics and Wearable Systems* 13948 (2026): 18, https://doi.org/10.1117/12.3089979.

19. N. Dalal, Y. Gu, D. R. Hines, A. Dasgupta, and S. Das, "Cracks in the 3D-Printed Conductive Traces of Silver Nanoparticle Ink," *Journal of Micromechanics and Microengineering* 29, no. 9 (2019): 097001, https://doi.org/10.1088/1361-6439/ab2f25.

20. A. Mostaccio and G. Marrocco, "Design, Prototyping, and Characterization of Laser-Induced Graphene Antennas on Flexible Substrates: Consolidating current knowledge," *IEEE Antennas and Propagation Magazine* 67, no. 6 (2025): 10–20, https://doi.org/10.1109/MAP.2024.3457309.

21. Y. Li and C. P. Wong, "Recent advances on electrical conductive adhesives (ECAs)," in 4th IEEE International Conference on Polymers and Adhesives in Microelectronics and Photonics (IEEE, 2004), 1–7, https://doi.org/10.1109/POLYTR.2004.1402732.

22. F. Bayat, M. Nazeri, G. Grau, and S. Pisana, "Encapsulating Laser-Induced Graphene to Preserve its Electrical Properties and Enhance its Mechanical Robustness," *Advanced Engineering Materials* 27, no. 22 (2025): 2501686, https://doi.org/10.1002/adem.202501686.

23. B. Asbani, K. Robert, P. Roussel, T. Brousse, and C. Lethien, "Asymmetric Micro-Supercapacitors Based On Electrodeposited Ruo2 and Sputtered VN Films," *Energy Storage Materials* 37 (2021): 207–214, https://doi.org/10.1016/j.ensm.2021.02.006.

24. A. Jrondi, G. Buvat, F. D. L. Pena, et al., "Major Improvement in the Cycling Ability of Pseudocapacitive Vanadium Nitride Films for Micro-Supercapacitor," *Advanced Energy Materials* 13, no. 9 (2023): 2203462, https://doi.org/10.1002/aenm.202203462.

25. D. M. Mattox, *Handbook of Physical Vapor Deposition (Pvd) Processing* (William Andrew, 2010).

26. M. I. Arefev, M. V. Shugaev, and L. V. Zhigilei, "Kinetics of Laser-Induced Melting of Thin Gold Film: How Slow Can It Get?," *Science Advances* 8, no. 38 (2022): abo2621, https://doi.org/10.1126/sciadv.abo2621.

27. L. Gallais, E. Bergeret, B. Wang, M. Guerin, and E. Bènevent, "Ultrafast Laser Ablation of Metal Films on Flexible Substrates," *Applied Physics A* 115, no. 1 (2014): 177–188, https://doi.org/10.1007/s00339-013-7901-2.

28. W. Wang, L. Lu, Z. Li, and Y. Xie, "Laser Induced 3D Porous Graphene Dots: Bottom-Up Growth Mechanism, Multi-Physics Coupling Effect and Surface Wettability," *Applied Surface Science* 592 (2022): 153242, https://doi.org/10.1016/j.apsusc.2022.153242.

29. J. M. Bennett and E. J. Ashley, "Infrared Reflectance and Emittance of Silver and Gold Evaporated in Ultrahigh Vacuum," *Applied Optics* 4, no. 2 (1965): 221, https://doi.org/10.1364/AO.4.000221.

30. R. E. Schmiedt, C. Qian, C. Behr, L. Hecht, A. Dietzel, and M. Sinapius, "Flexible Sensors on Polymide Fabricated by Femtosecond Laser for Integration in Fiber Reinforced Polymers," *Flexible and Printed Electronics* 3, no. 2 (2018): 025003, https://doi.org/10.1088/2058-8585/aabe45.

31. P. Chen, Y. Xin, H. Zu, et al., "Laser-Stepwise-Induced Graphene With Reduced Sheet Resistance Enables Electromagnetic Shielding Manipulation," *Nano Research* 18, no. 11 (2025): 94908018, 10.26599/NR.2025.94908018.

32. A. Lazaro, M. R. Cujilema, R. Villarino, M. Lazaro, and D. Girbau, "A Novel Approach for Wine Anti-Counterfeiting Using Laser-Induced Graphene Chipless RFID Tags on Cork," *Scientific Reports* 15, no. 1 (2025): 12750, https://doi.org/10.1038/s41598-025-97613-z.

33. X. Liu, J. Choi, Z. Xu, C. P. Grey, S. Fleischmann, and A. C. Forse, "Raman Spectroscopy Measurements Support Disorder-Driven Capacitance in Nanoporous Carbons," *Journal of the American Chemical Society* 146, no. 45 (2024): 30748–30752, https://doi.org/10.1021/jacs.4c10214.

34. A. C. Ferrari and J. Robertson, "Interpretation of Raman spectra of disordered and amorphous carbon," *Physical Review B* 61, no. 20 (2000): 14095–14107, https://doi.org/10.1103/PhysRevB.61.14095.

35. L. Huang, H. Wang, P. Wu, et al., "Wearable Flexible Strain Sensor Based on Three-Dimensional Wavy Laser-Induced Graphene and Silicone Rubber," *Sensors* 20, no. 15 (2020): 4266, https://doi.org/10.3390/s20154266.

36. B. Kulyk, B. F. R. Silva, A. F. Carvalho, et al., "Laser-Induced Graphene from Paper for Mechanical Sensing," *ACS Applied Materials & Interfaces* 13, no. 8 (2021): 10210–10221, https://doi.org/10.1021/acsami.0c20270.

37. A. M. Barja, Y. K. Ryu, S. Tarancón, et al., "Laser-Induced Graphene Strain Sensors for Body Movement Monitoring," *ACS Omega* 9, no. 37 (2024): 38359–38370, https://doi.org/10.1021/acsomega.3c09067.

38. S. Aftab, G. Koyyada, M. Mukhtar, et al., "Laser-Induced Graphene for Advanced Sensing: Comprehensive Review of Applications," *ACS Sensors* 9, no. 9 (2024): 4536–4554, https://doi.org/10.1021/acssensors.4c01717.

Supporting Information

Additional supporting information can be found online in the Supporting Information section.

Supporting File: aelm70576-sup-0001-SuppMat.pdf.

2199160x, 0, Downloaded from https://advanced.onlinelibrary.wiley.com/doi/10.1002/aelm.70576 by CochraneItalia, Wiley Online Library on [26/10/2026]. See the Terms and Conditions (https://onlinelibrary.wiley.com/terms-and-conditions) on Wiley Online Library for rules of use; OA articles are governed by the applicable Creative Commons License